PHYSICAL SCIENCES

Ultrasonic cavitation shock wave exfoliation dynamics of 2D materials revealed in situ by MHz XFEL imaging and multiphysics modeling

Kang Xiang[1]†, Ling Qin[1,2]†, Shi Huang[1,3], Hongyuan Song[1], Vasilii Bazhenov[4], Valerio Bellucci[4], Sarlota Birnšteinová[4], Raphael de Wijn[4], Jayanath C. P. Koliyadu[4], Faisal H. M. Koua[4], Adam Round[4], Ekaterina Round[4], Abhisakh Sarma[4], Tokushi Sato[4], Marcin Sikorski[4], Yuhe Zhang[5], Eleni Myrto Asimakopoulou[5], Pablo Villanueva-Perez[5], Kyriakos Porfyrakis[6], Iakovos Tzanakis[7], Dmitry G. Eskin[8], Nicole Grobert[9], Adrian P. Mancuso[4,10,11], Richard Bean[4], Patrik Vagovič[4,12], Jiawei Mi[1]*

Using megahertz x-ray free electron laser imaging with x-ray pulses of ~25 femtoseconds and a machine-learning strategy, we have conducted comprehensive in situ imaging studies on the dynamics of cavitation bubble clouds in ultrasound fields at the SPB/SFX beamline of the European XFEL. The research unambiguously revealed the quasi-simultaneous implosion of multiple bubbles and simultaneous collapse of bubble cloud in nanosecond scale and their dynamic impacts onto two-dimensional (2D) materials for layer exfoliation. We have also performed multiphysics modeling to simulate the shock wave emission, propagation, impact, and stresses produced. We elucidated the critical conditions for producing instant or fatigue exfoliation and the effects of bonding strengths and structural defects on the exfoliation rate. The discoveries have filled the long-standing missing knowledge gaps in the underlying physics of exfoliating 2D materials in ultrasound fields, providing a solid theoretical foundation for optimizing and scaling-up operation to produce 2D materials in a much more cost-effective and sustainable way.

INTRODUCTION

Cavitation bubbles are vapor-filled cavities (or voids) in a continuous liquid medium, which are generated when a local volume within a liquid is subjected to sufficiently low pressure. These phenomena are commonly found in nature (rivers, lakes, oceans, etc.) and in man-made engineering systems (pumps, propellers, chemical mixing machines, etc.) (*1*, *2*). When high-power acoustic waves are applied into a liquid, hundreds to thousands of cavitation bubbles (often called a bubble cloud) could be produced in the regions with sufficient variation of acoustic pressure. Although a huge number of studies have been conducted on the dynamic evolution of a single bubble (its initiation, growth, oscillation, and implosion) in a liquid-bubble system (*3*), systematic research activities on the dynamic behavior of bubble clouds have been very limited because of the challenges of conducting suitable experimental observations and the prohibitive cost, time, and complexity for performing meaningful numerical simulations. However, an in-depth and comprehensive understanding of bubble cloud dynamics would have profound impacts on many physical, biological, and environmental disciplines (*3*). Currently, one strategically important, green, and sustainable modern development is the uses of ultrasound to enable highly efficient, low-cost, and environmentally friendly chemical synthesis and processing of structural and functional materials (*4*, *5*). Among these, two-dimensional (2D) functional materials have many unique and superior optical, electrical, and magnetic properties and have enormous application potentials in energy storage, catalysis, and nanoelectronics (*6*–*9*). The current challenge of manufacturing 2D materials is to develop efficient, cost-effective, and sustainable technologies for making large 2D sheets in substantial quantities (*10*–*15*). Ultrasound liquid phase exfoliation (ULPE) has been identified as one of the most promising environmentally friendly and low-cost technical routes for producing 2D large-size multilayers (typically ~1 μm lateral size and ~1 to 10 atomic layers thick) with far fewer defects and less surface oxidation compared to other routes, e.g., mechanical cleavage or chemical vapor deposition (*14*–*16*).

In the ULPE process, there are complex and dynamic interactions among the solvent, cavitation bubbles, ultrasonic shock waves, and 2D solid materials across multilength (nanometers to millimeters) and multitime (nanoseconds to seconds) scales (*4*, *17*–*20*). Extensive research has been carried out in the past decades to understand the dynamic links between cavitation bubble dynamics, shock wave generation, and propagation, as well as layer exfoliation (*4*, *5*, *17*, *21*, *22*). For example, Li (*23*) suggested that the ultrasonic bubbles produced in sonication broke the graphene sheets into nanofragments. Cravotto (*10*) and Alaferdov (*24*) pointed out that cavitation-induced shock

[1]School of Engineering and Technology, University of Hull, Cottingham Road, Hull HU6 7RX, UK. [2]Center of Innovation for Flow through Porous Media, Department of Energy and Petroleum Engineering, University of Wyoming, Laramie, WY 82071, USA. [3]School of Engineering and Westlake Institute for Advanced Study, Westlake University, Hangzhou 310030, China. [4]European XFEL, Holzkoppel 4, 22869 Schenefeld, Germany. [5]Synchrotron Radiation Research and NanoLund, Lund University, Box 118, 221 00 Lund, Sweden. [6]Center for advanced manufacturing and materials (CAMM), Faculty of Engineering and Science, University of Greenwich, Central Avenue, Chatham Maritime, Kent ME4 4TB, UK. [7]School of Engineering, Computing and Mathematics, Oxford Brookes University, College Cl, Wheatley, Oxford OX33 1HX, UK. [8]Brunel Center for Advanced Solidification Technology, Brunel University of London, Kingston Lane, London UB8 3PH, UK. [9]Department of Materials, University of Oxford, Parks Road, Oxford OX1 3PH, UK. [10]Department of Chemistry and Physics, La Trobe Institute for Molecular Science, La Trobe University, Melbourne, Victoria, Australia. [11]Diamond Light Source Ltd., Harwell Science and Innovation Campus, Didcot OX11 0DE, UK. [12]Center for Free-Electron Laser Science CFEL, Deutsches Elektronen-Synchrotron DESY, Notkestr. 85, Hamburg 22607, Germany.
*Corresponding author. Email: j.mi@hull.ac.uk
†These authors contributed equally to this work.

waves exerted high elastic acoustic energy on the graphite sheets to facilitate exfoliation. Lotya (*25*) reported that the shock waves produced at the collapse of bubbles could act on the crystal edges, overcoming the van der Waals bonds between adjacent layers. Despite these advances, currently, there is no experimental technique capable of resolving the dynamics of atomic-layer exfoliation under ultrasonic cavitation in real time. Techniques such as transmission electron microscopy or atomic force microscopy offer nanometer resolution but are inherently limited to postmortem imaging or steady-state probing and thus cannot capture the ultrafast transient nature of cavitation bubble and graphite interactions (*26*). Our very recent in situ and real-time studies using ultrafast synchrotron x-ray (*4*, *18*) and high-speed optical imaging (*17*, *27*) indicated that graphite layer exfoliation under ultrasound is a far more complicated process than previously proposed. The onset and growth of the exfoliated layers often occurred in a cyclic fatigue manner closely linked to the amplitude and time of the ultrasonic waves applied (*4*). However, because of the limited spectral brightness (brilliance) of the synchrotron sources at the imaging rate of megahertz or higher, the nanosecond timescale and nanometer-length scale layer exfoliation dynamics at the instant of bubble implosion and shock wave impact have never been clearly revealed. Hence, many fundamental issues in this field remain unsolved and are still subject to intense debates. Recently, we used the megahertz x-ray microscopy (*28*–*30*) available at the European X-ray Free Electron Laser (EuXFEL), Schenefeld, Germany (see Fig. 1 and fig. S4) to study the highly transient phenomena of ultrasonic bubble implosion, shock wave propagation, and their effects on the onset of layer exfoliation and subsequent layer growth dynamics in two different graphite materials, i.e., highly oriented pyrolytic graphite sheets (HOPG) and natural graphite flakes (NGFs).

The femtosecond x-ray pulses produced at the EuXFEL have a typical peak brilliance of 10^{33} photons s^{-1} mm^{-2} $mrad^{-2}$/0.1% bandwidth (~10^9 times brighter than those from the third- or fourth-generation synchrotron sources). Such extremely brilliant femtosecond pulses coupled with a tunable pulse train structure allowed us to take x-ray images at megahertz frame rate without motion blur, which is often found in the synchrotron x-ray images when operated in the megahertz domain. We integrated the megahertz x-ray microscopy with our unique ultrasound processing unit at the SPB/SFX (single particles, clusters, and biomolecules and serial femtosecond crystallography) instrument of the EuXFEL and collected ~4.9 TB of x-ray movies in carefully designed and well-controlled experimental conditions. We have systematically captured at a micrometer-nanosecond resolution the highly transient dynamic phenomena, including the nucleation of ultrasonic cavitation bubbles, their growth and implosion, the onset of local shock waves, as well as their propagation and impact onto the graphite materials. Using a dedicated machine learning (ML) strategy, we performed comprehensive analyses on those TB of image data and extracted the most important scientific evidence, which is indispensable for implementing multiphysics numerical simulation. This approach enables us to reconstruct the evolution of stress fields at the graphite interface and to identify the defect-amplified stress concentrations that are sufficient to exceed the interlayer bonding threshold, thereby providing a physically consistent cross-scale link to molecular exfoliation processes. For example, movie S1 (all movies are in the Supplementary Materials) contains the typical full-frame x-ray images selected from the consecutive trains (the intertrain images, i.e., one image from one train), and movie S2 contains the typical full-frame images within one pulse train (the intratrain images) for the HOPG. Movies S3 and S4 contain the corresponding images for the NGF cases. Such comprehensive and synergistic studies have allowed us to fully reveal and elucidate the complex and coupled underlying physics in ultrasound exfoliation of graphite materials. In particular, how powerful local shock waves were produced by the collective implosion of the cavitation bubble cloud, and how such shock waves produced differential impulsive and cyclic stresses onto the graphite layers, which was the most dominant driving force for the layer exfoliation and closely linked to the structure defects of the graphite materials. These discoveries have filled the long-standing knowledge gaps in this very important research field. The findings are critical for the

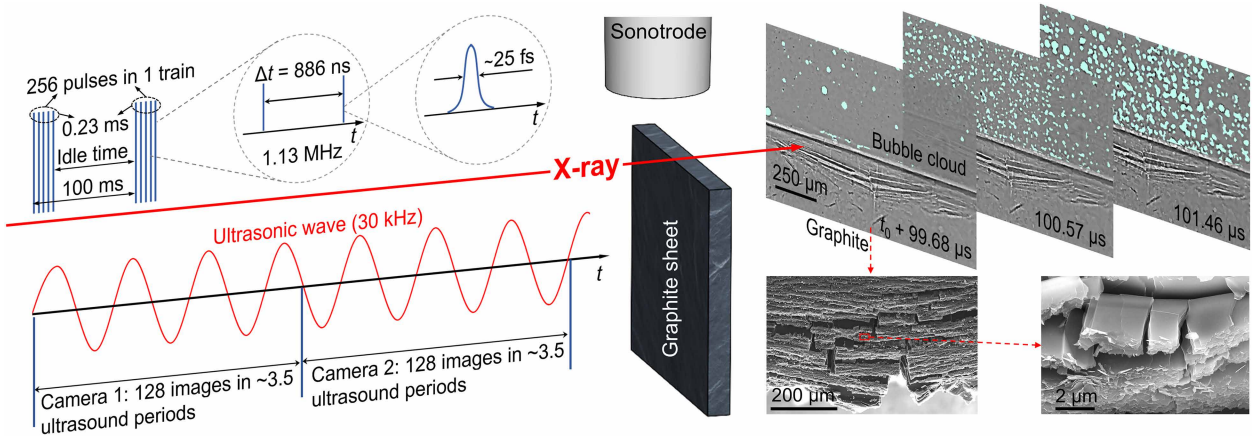

Fig. 1. The megahertz x-ray microscopy and x-ray pulse train configurations. From left to right: The x-ray (20 keV) pulse train structures. Each train contains 256 pulses (25-fs duration for each pulse) with 886-ns interval between two consecutive pulses, providing an intra-burst frame rate of ~1.13 MHz. Two Shimadzu HPV-X2 cameras were used, each recorded 128 images in ~3.5 ultrasound periods. The field of view is 1280 μm (horizontal) by 800 μm (vertical) with an effective pixel size of 3.2 μm. The sonotrode tip was positioned 1 to 2 mm above the graphite sample. Typical x-ray images show the bubble clouds and the shock wave impact at the graphite top surface, exfoliating multiple graphite layers at nanosecond timescale. The scanning electron microscopy images show the exfoliated graphite layers consisting of many sub-micrometer lamellae after ULPE processing.

optimization and scale-up of ULPE for producing 2D materials in a much more efficient, cost-effective, and sustainable way.

RESULTS

The shock wave produced by a single bubble and its interaction with a graphite layer

Figure 2 (A and B) shows the implosion dynamics of a single bubble (see movie S5 for the full set of images; fig. S7 also clearly shows where the images of Fig. 2A were cropped from). Clearly, a near-circular bubble with an initial radius of ~50 μm underwent violent contraction. Typical distorted bubble patterns (C shape) were repeatedly observed, indicating the onset of instability at the circular bubble boundary under the alternating pressure field, and these were the precursors of bubble implosion. Figure 2C shows the simulated implosion dynamics of a single bubble (detailed in sections S1.1 and S1.2 of the Supplementary Materials), illustrating the emission and propagation of the shock waves at the instant of bubble implosion. The pressure contour maps in Fig. 2C and the pressure wave propagation as a function of time and distance (Fig. 2E) indicate that the maximum pressure at the bubble implosion center reached ~5.0 MPa with a duration of ~20 μs. At a distance of 1000 μm from the center, the pressure very rapidly decayed to below ~0.8 MPa.

Figure 2D (movie S6) shows another typical case where a single bubble was imploding near a graphite layer (fig. S8 also shows clearly where the images were cropped from). The implosion caused the layer to be deflected instantly. Unlike the implosion of a free bubble (i.e., without any nearby obstacle), the bubble was spatially constrained by the graphite, resulting in a distorted elliptical shape. The simulation (Fig. 2F) shows that the impulsive stress due to the shock wave impact at the graphite surface reached ~1.5 MPa, causing the graphite layer to be deflected by ~3.3 μm in 2.67 μs, with a peak deflection velocity of ~1.4 μm/μs.

The shock wave produced by multiple bubbles and the interactions with a graphite layer

Figure 3 (A and B) (also see movie S7) show the implosion dynamics of three bubbles, and Fig. 3C shows the simulated shock wave emission and propagation. Figure 3A shows that, when the first bubble imploded, the other two bubbles imploded successively and fractured into several smaller bubble fragments in a period of ~10 μs (from the second to the fifth images). Clearly, there existed a very short time gap (i.e., ~5 μs) between the implosion events of different bubbles. Such quasi-simultaneous implosion events result from rapidly evolving, highly complex local conditions including oscillatory acoustic pressure field, secondary pressure waves, microjet-induced perturbations, and bubble-bubble hydrodynamic interactions, etc., which occur too quickly to be clearly captured even with megahertz imaging. The complementary simulation results (Fig. 3, C and E) indicate that, compared to the single bubble case, the shock waves produced by the multiple bubble implosion generated three pressure peaks (with varied intensity) due to the interference of the local pressure waves produced by each individual bubble, inducing some form of instability or resonance. The maximum peak pressure could reach ~6.0 MPa because of one bubble implosion that perturbs the pressure condition for "triggering" the next bubble implosion.

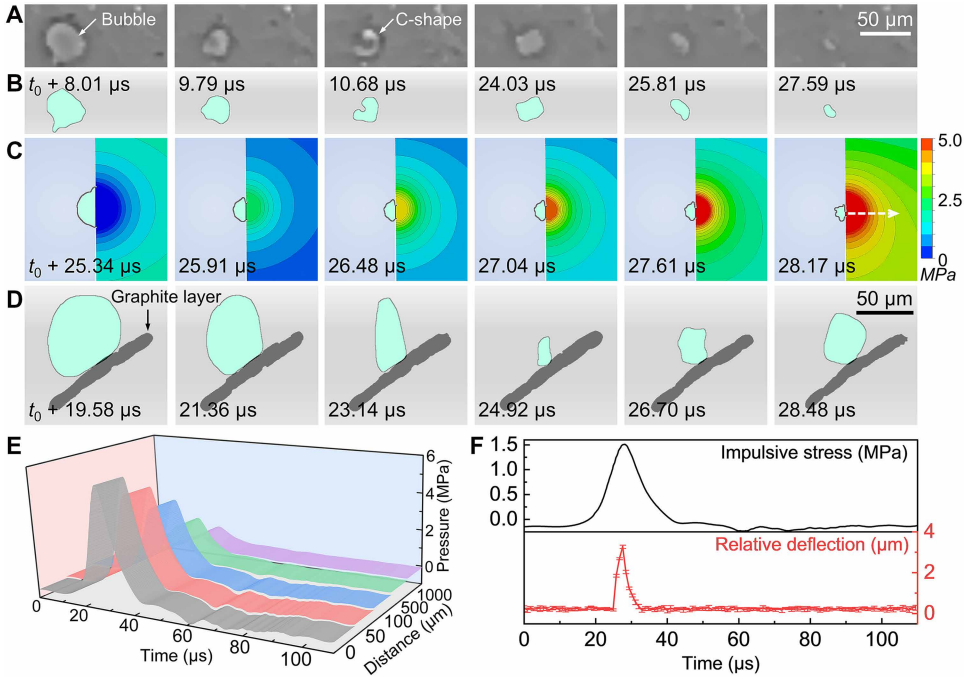

Fig. 2. The implosion dynamics of a single bubble, the shock wave propagation, and its interaction with a graphite layer. (**A**) The typical raw x-ray images and (**B**) the corresponding ML-processed and binarized images (see movie S5), showing the implosion dynamics of a single bubble. (**C**) The simulated bubble implosion dynamics (left half) and pressure fields (right half). The propagation fronts of the shock waves were indicated by the pressure contour lines. (**D**) The dynamic interactions between a single bubble and a graphite layer (see movie S6), showing the deflection of the graphite layer caused by the shock wave impact. (**E**) The calculated pressure profiles as a function of time and distance. 0, 50, 100, 500, and 1000 μm from the bubble implosion center as indicated by the arrow in (C). (**F**) The time-evolved impulsive stress and relative deflection of the graphite layer shown in (D).

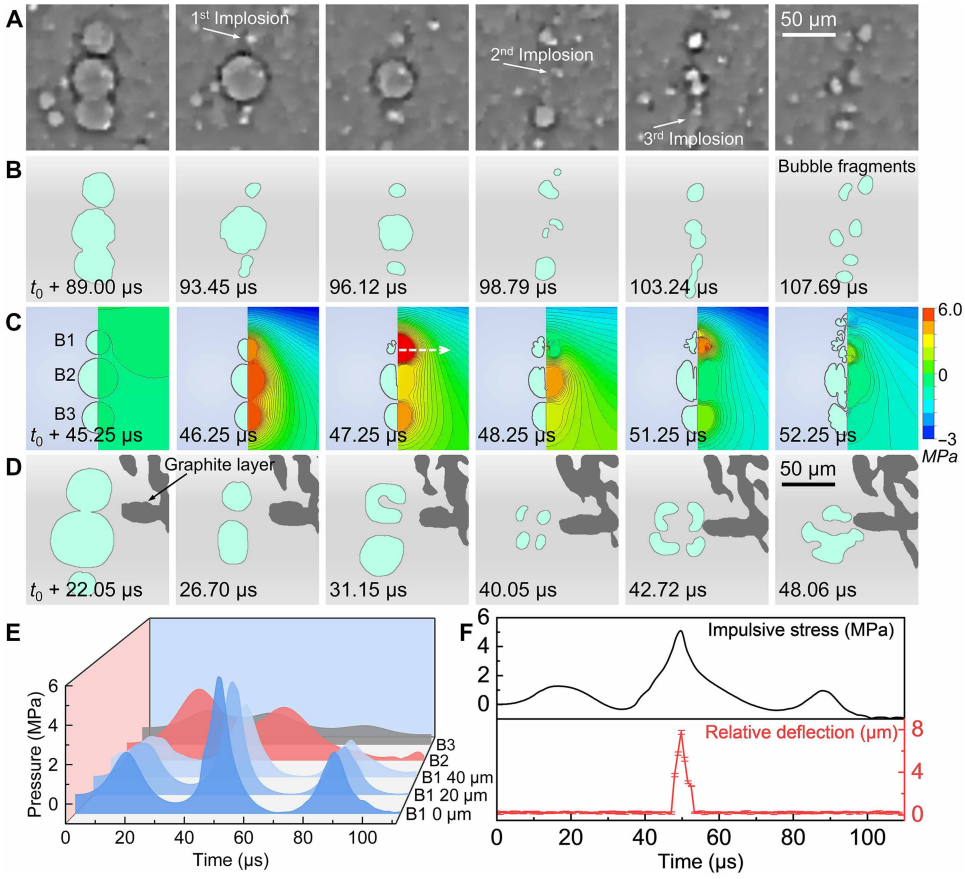

Fig. 3. Shock wave produced by the implosion of multiple bubbles and the interaction with a graphite layer. (**A**) The typical normalized x-ray images and (**B**) the corresponding ML-processed and binarized images (see movie S7), showing the implosion dynamics of three bubbles. (**C**) The simulated bubble implosion dynamics (left side) and pressure fields (right side). The propagation fronts of the shock waves were indicated by the pressure contour lines. (**D**) The dynamic interactions between the bubbles and the graphite layer (see movie S8), showing the deflection of the graphite layer caused by the shock wave impact. (**E**) The calculated pressure waves as a function of time and distance for different bubbles. B1 (0 μm), B1 (20 μm), and B1 (40 μm) are the horizontal distances from the bubble B1 implosion center, as indicated by the white arrow in (C). These bubble implosions occur within microseconds of each other, likely due to local pressure perturbations amplified by earlier collapses. (**F**) The time-evolved impulsive stress and relative deflection of the graphite layer shown in (D).

Figure 3D (movie S8) shows a typical scenario of shock wave impact at the graphite layer. When the first shock wave arrived, the graphite layer deflected very slightly. However, the second shock wave generated the strongest impact force, deflecting the graphite layer instantly by ~7.8 μm. The instantaneous deflection velocity reached ~3.1 μm/μs, and the highest impulsive stress in the graphite layer was calculated to be ~5.0 MPa (Fig. 3F).

The shock wave produced by bubble cloud collapse and the effect on layer exfoliation

In a fully developed ultrasonic cavitation zone, there exist hundreds or even thousands of micrometer-sized bubbles depending on the size of the cavitation zone. The megahertz imaging technique allowed us to systematically image and study the bubble cloud implosion dynamics. However, it is virtually impossible to perform sensible numerical simulations. Hence, we again used the machine leaning–assisted strategy to analyze the bubble cloud characteristics, i.e., calculating the evolution of bubble numbers (the area fraction of the bubbles in a representative field of view) as a function of pressure and time.

Figure 4B (movie S9) shows the number and area of the bubbles in a representative area in the cavitation zone as function of amplitude and time in ~3.5 ultrasound periods (Fig. 4A). Clearly, the second image in Fig. 4B shows that most of the bubbles imploded at that moment (i.e., $t = t_0 + 3.56$ μs). Hence, the number of bubbles and the bubble area fraction reached their minimum values, indicating the arrival of the superposed shock waves due to the simultaneous collapse of the bubble cloud. Under the influence of such shock wave impact, the graphite layer deflected significantly downward by ~11.0 μm (Fig. 4C) with a peak instantaneous velocity of ~3.7 μm/μs (Fig. 4D). Subsequently, the third image in Fig. 4B shows that most bubble fragments produced by such collapse appeared again, starting to regrow and expand into a relatively mature bubble cloud again in the next ~3 ultrasound periods. At $t = t_0 + 99.68$ μs (the ninth image in Fig. 4B), the bubble cloud collapsed again, producing similar shock waves and a similar level of deflection onto the graphite layer. The observed deflection events occurred within ~0.89 μs following the collective collapse of bubble clouds. Given that the distance from the sonotrode tip to the graphite surface was set as ~1 mm, we can estimate a shock wave propagation speed of ~1.12 mm/μs

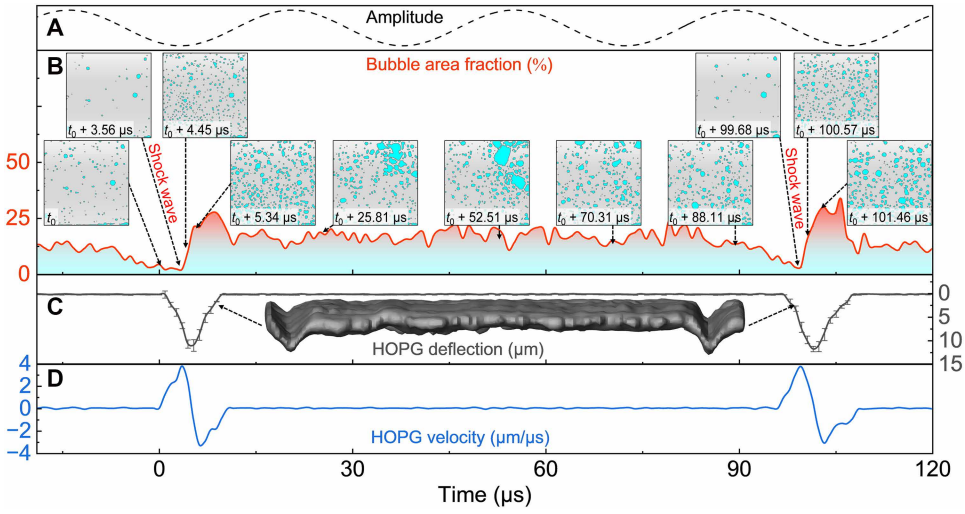

Fig. 4. The shock wave produced by the simultaneous collapse of bubble cloud and the effect on HOPG layer exfoliation. (**A**) The amplitude of the ultrasound applied. (**B**) The calculated bubble area fraction as a function of amplitude and time. (**C**) The relative deflection and (**D**) velocity of the HOPG layer versus time. The inset in (C) shows the cross-sectional view of the deflection of the HOPG layer. Please see fig. S11 and movie S9 for more details of the bubble evolution and HOPG layer exfoliation dynamics.

(i.e., ~1120 m/s), which is comparable to the previous measurement results (*31*). Such cyclic arrivals of the shock wave impact were clearly shown in movie S9. While between the arrivals of the two superposed shock waves, the bubble clouds oscillated continuously or imploded without producing any sensible shock waves (see the fourth to eight images in Fig. 4B); hence, the graphite layers only vibrated gently in a scale of 0.1 to 0.3 μm, with a mean deflection velocity of ~0.1 μm/μs (Fig. 4, C and D). Such clear and unambiguous evidence from the megahertz images provides a convincing argument that the locally superposed shock waves produced by the bubble cloud collapse are the predominant driving force for producing layer exfoliation.

Figure 5 (movie S10) shows another typical case of NGF exfoliation in one pulse train, which is a very similar scenario to that of the HOPG. When the superposed shock waves arrived (the second image in Fig. 5B, i.e., $t = t_0 + 50.73$ μs), the rightmost graphite layer bundle deflected by ~11.7 μm in 2.67 μs, with a peak velocity of ~4.7 μm/μs (Fig. 5, C and D, and more vividly in movie S10). However, in the next tens of microseconds, the opened graphite layer bundle did not bounce back immediately but continued to sway sideways until the next shock waves arrived. In addition, Fig. 5C also shows that another deflection event occurred at $t = t_0 + 153.97$ μs, following a subharmonic periodicity of ~3 ultrasound periods, which is highly consistent with the observations in the HOPG case (Fig. 4).

Shock wave propagation, interference, and the impact force acting on graphite multilayers

We used a density-based solver to simulate the shock wave propagation in deionized water (DIWater) and a fluid-structure interaction model to calculate the shock waves' impact forces and the stresses produced into the graphite multilayers (the three submodels are described in sections S1.1, S1.2, and S1.3 of the Supplementary Materials). Using the shock waves produced by three bubbles as a typical case, Fig. 6Aa shows the initial points where the shock waves started (for a tractable simulation, we assumed that the shock waves started at the same height along a horizontal line). The numerical model assumes simultaneous bubble implosion to represent an ideal case for shock wave emission, propagation, and superposition. Although this does not replicate the exact timing observed in experiments, it enables quantification of the maximal impulsive stress transmitted to the graphite interface. According to our previous measurements, the initial shock wave pressure was set as 7 MPa (*17*). The traveling distance to graphite layer top surface was set as 1 mm. Figure 6 (B and C) shows the geometry and results of the modeling. The first one was a thin plate of five well-bonded layers (0.5 μm thick for each layer) to represent multilayer graphite without defects (Fig. 6B and fig. S16A). The second one was a similar thin plate but with a microcrack of 1 μm deep at the center to represent the multilayer structure with defects (Fig. 6C and fig. S16B).

Figure 6A shows the simulated propagation of the superposed shock waves in DIWater. The interference of the three shock waves resulted in complex, unevenly distributed pressure contour maps with alternating negative and positive pressure bands during propagation (Fig. 6, Ab to Ad, shows the rapidly changed pressure directions and amplitudes). After the shock waves impacted onto the graphite top surface, Fig. 6 (B and C) shows the 3D view of the stress distribution of the graphite multilayers without and with defect when subjected to the maximum impact stresses of 6.6 to 7.4 MPa. Figure 6 (D and E) shows the time-evolved impulsive stresses. Clearly, for a perfectly aligned graphite multilayers without any defect, the peak impulsive stress at the surface (i.e., P1) was ~6.6 MPa and that at 1 μm below (P2) was ~5.8 MPa, indicating that there is no notable stress difference in between (Fig. 6D), while, if a microcrack defect of just 1 μm deep was present, the stress concentration effect (see sections S1.5 to S1.7 of the Supplementary Materials) could increase the local stresses at the sharp tip (P4) and the edge area (P5) to 7.2 and 7.4 MPa. Such amplified stress concentration introduced effective shear stress that ran parallel to the layers, which very effectively promoted instant layer exfoliation (*4*, *17*, *32*), i.e., at the moment when the superposed shock waves arrived and impacted onto the graphite layer. Furthermore, the rapidly changed pressure directions and amplitudes also produced very effective high-frequency

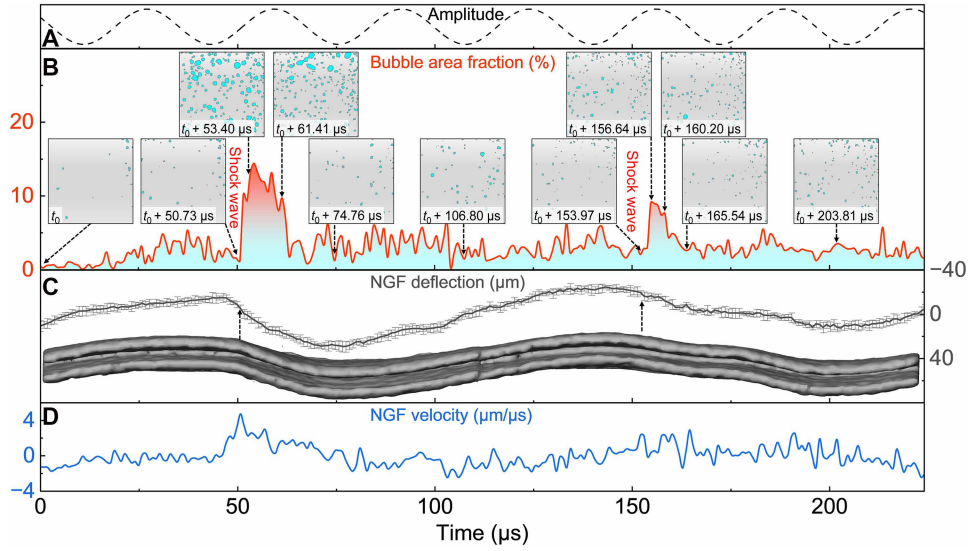

Fig. 5. The shock wave produced by the simultaneous collapse of bubble cloud and the effect on NGF layer exfoliation. (**A**) The pressure amplitude of the ultrasound applied. (**B**) The calculated bubble area fraction as a function of pressure and time. (**C**) The relative deflection and (**D**) velocity of the NGF layer bundle versus time. The inset in (C) shows the cross-sectional view of the deflection of the NGF layer bundles. Please see fig. S12 and movie S10 for more details of the bubble evolution and NGF layer exfoliation dynamics.

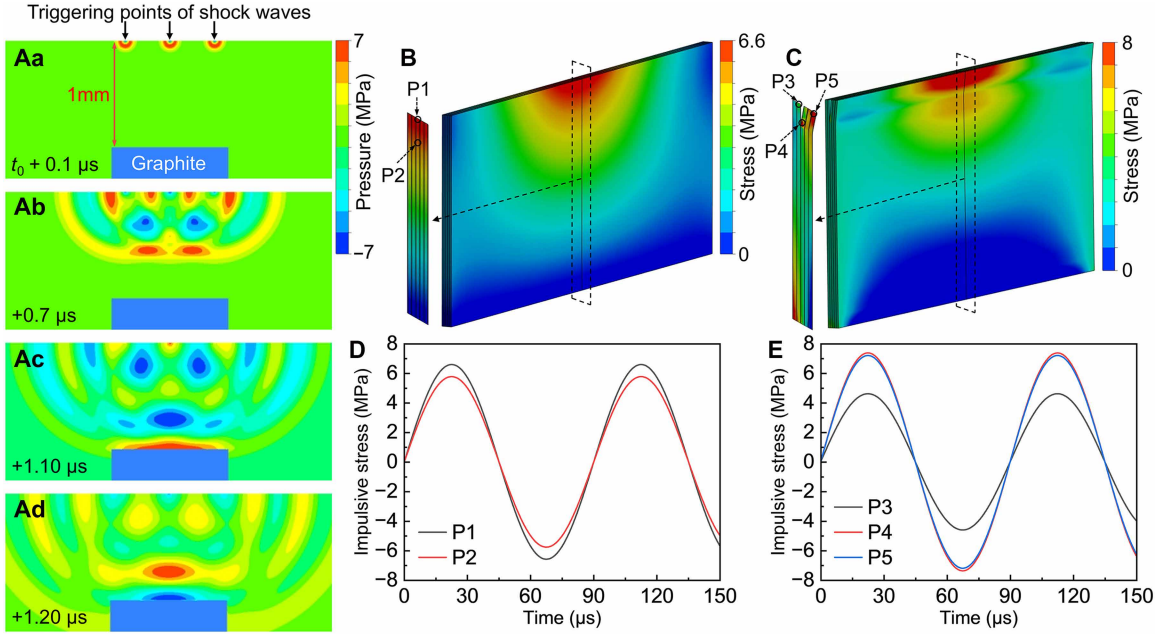

Fig. 6. The simulated shock wave propagation and their impact on the graphite multilayers without and with defects. (**A**) The simulated pressure contour maps generated by the propagation of superposed shock waves at a traveling distance of 1.0 mm. Simultaneous bubble implosion was assumed here, representing an ideal case for shock wave emission, propagation, and superposition. The peak impulsive stress distribution inside the graphite multilayers: (**B**) without defect; (**C**) with defect. The time-evolved alternating impulsive stress acting on the graphite surface: (**D**) positions P1 and P2 in (B); (**E**) positions P3, P4, and P5 in (C). The time-evolved stress contour map in one ultrasound period is shown in movie S11 for the case without defect and movie S12 for the case with defect.

fatigue effect on the graphite layers under cyclic impact, making the cavitation shock wave–enabled layer exfoliation to be the most efficient method in opening up and delaminating the graphite layers, especially for those materials with high density of defects, e.g., the NGFs.

The dominant driving force for layer exfoliation due to bubble cloud implosion

The results of the megahertz x-ray imaging and simulation have demonstrated clearly and convincingly the role of quasi-simultaneous implosion of multiple bubbles and simultaneous collapse of bubble cloud in terms of producing powerful shock waves and impulsive stresses onto the graphite layers. The shock wave produced by a single bubble implosion can generate stress in the scale of ~1.1 MPa, which only deflected the graphite layer bundles with a modest deflection velocity of ~1.0 μm/μs (see fig. S18A). Even when the bubble imploded near the surface of the graphite layers, it will not be sufficiently enough to produce any sensible layer exfoliation (*4*). In contrast, quasi-simultaneous implosion of multiple bubbles and simultaneous collapse of bubble clouds produced superposed shock waves with impact stresses up to ~6.6 MPa, causing graphite layers deflection at a velocity of ~2.6 μm/μs (see fig. S18A). The bubble cloud collapse exhibited a regular subharmonic periodicity of ~3 ultrasound periods. Such periodical renucleation and collapse of bubble clouds produced amplified and repeated impact forces, leading to a self-sustaining layer exfoliation cycle in the long run.

The effects of defects and interlayer bonding strength on layer exfoliation

Structural defects and interlayer bonding strength are two other crucial factors in determining the layer exfoliation dynamics and exfoliation rate. We imaged and observed the exfoliation behavior of the HOPG and NGF over a long-time period (hundreds to thousands of seconds; see fig. S17) under the impacts of cyclic shock waves. The mean exfoliation rate for the HOPG was only ~0.06 μm/s, whereas that of the NGF was ~2.34 μm/s (with a peak instant exfoliation often found at ~38 μm/s), ~40 times higher than that of the HOPG (fig. S18B). The key difference is attributed to the fact that the HOPG has high crystallographic ordering and minimal structural defects. In reality, the shock wave impact may come from all different directions relative to the bonded graphite layers. As a result, although the calculated impact stresses from the shock waves are in the similar scale to the layer bonding strength of the HOPG, the effective stresses that can cause layer exfoliation (i.e., the resulting tensile forces perpendicular to the layers or the shear forces along the layers) are in the range of 30 to 50% of the impact stresses, much lower than the HOPG layer bonding strength (~5.0 MPa). Hence, repeated shock wave impacts over a longer time are needed to create fatiguetype layer exfoliation. The exfoliation length and rate shown in fig. S17 (A and B) provide convincing evidence for such an argument. In contrast, the NGF has much lower interlayer bonding strength (~0.48 MPa). The high-density defects are naturally preexisting cracks that enhance the stress concentration effects. Most of the shock waves from all directions can produce sufficient tensile or shear forces that are able to open up the NGF layers instantly at the impact (see fig. S17, C and D), causing an instant exfoliation rate up to ~40 times higher than in the HOPG case.

DISCUSSION

In this study, by taking full advantage of the ultrashort x-ray pulses (~25 fs) with a unique pulse train structure at the EuXFEL, we have conducted systematic and comprehensive operando imaging studies on the layer exfoliation dynamics of 2D graphite materials in ultrasound fields. We have imaged and quantified, at nanosecond timescale and micrometer length scale simultaneously, the local shock waves produced by the implosion of a single cavitation bubble, multiple bubbles, and bubble clouds, as well as the layer exfoliation dynamics under such shock wave impacts. Multiphysics modeling was also carried out to simulate shock-wave emission and propagation, as well as the impact and stresses produced in the materials.

The pressures produced in the liquid at bubble implosion are the source of the energy (or force) for generating impulsive stresses in the graphite layers. Our work has demonstrated that the magnitude of such impulsive stress is dependent on (i) the magnitude of bubble implosion, i.e., due to a single bubble, multiple bubbles, or bubble cloud; (ii) the distance between the implosion center and the graphite layer, and (iii) any surface defects on the graphite layers. Typically, the shock wave produced by a single bubble implosion is in the range of 4.0 to 5.0 MPa at or near the implosion center. The resulting average impulsive stress transmitted to the nearby graphite layer is ~1.1 MPa, insufficient to cause any appreciable layer exfoliation. The quasi-simultaneous implosion of multiple bubbles and simultaneous collapse of bubble clouds result in the superposition of shock waves, which can significantly amplify the impulsive stress up to ~6.6 MPa. When any defects (or cracks) exist on the graphite surface, the geometrical stress concentration effect can increase the stress significantly (e.g., ~7.4 MPa in the case of Fig. 6E). Such enhanced and superposed stresses exceed the interlayer bonding threshold (*4*, *17*) and initiate graphite layer exfoliation effectively.

Structural defects and interlayer bonding strength are two paramount materials properties in determining the layer exfoliation rate. The mean exfoliation rate for the HOPG is only ~0.06 μm/s, whereas that of the NGF is ~2.34 μm/s. Because of the high strength and near-perfectly bonded layer structure with minimum defects, the layers in the HOPG are mainly exfoliated because of the fatigue effect. The higher density defects on the NGF often result in immediate and instant exfoliation with a maximal rate of up to ~38 μm/s, ~40 times higher than that of the HOPG.

For the bubble cloud–produced shock waves, they exhibit inherent subharmonic periodicity of ~3 ultrasound periods as revealed by the megahertz imaging. Such periodic nature of the powerful shock waves due to the simultaneous collapse of bubble cloud is the unique advantage and characteristic of ULPE. It enables highly efficient, self-sustaining continuous layer exfoliation compared to other mechanical shear–based exfoliation processes.

To summarize, these findings provide not only a mechanistic understanding of the cavitation shock wave–induced exfoliation but also practical guidance for the experimental optimization of 2D material production. Specifically, the results suggest that promoting collective bubble cloud collapse to achieve superposed shock waves, leveraging subharmonic periodicity for fatigue-driven exfoliation, and selecting or engineering graphite precursors with lower interlayer bonding strength and higher defect density can greatly promote the exfoliation efficiency and reduce lead times. Such insights offer a physics-based foundation for tuning ultrasonic parameters and material design strategies in scalable, cost-effective exfoliation processes.

MATERIALS AND METHODS

Materials

The two different graphite materials used in the experiments are as follows: (i) HOPG, 10 mm by 10 mm by 1.5 mm, purchased from Agar Scientific Ltd.; and (ii) NGF, 2 mm by 3 mm by 0.2 to 0.4 mm, purchased from Sigma-Aldrich. The HOPG has high crystallographic orientation and low defect density with typical interlayer bonding strength of 5.0 MPa (*33*). The NGF is extracted directly from the mineral and usually retains some typical defects (i.e., cracks and edge defects, etc.) from the natural formation process. The NGF's interlayer bonding strength is in the range of 0.25 to 0.75 MPa, with the average value of 0.48 MPa (*34*–*36*), which is ~10 times weaker than that of HOPG. We deliberately choose the two different graphite materials to study the exfoliation dynamics due to the difference in bonding strength and structural defects. Figures S1 and S2 show the typical macroscopic images of the raw materials and the scanning electron microscopy images of the exfoliated graphite multilayer bundles after ULPE.

To mount the graphite samples for the in situ ULPE experiments, we firstly cut a rectangular piece (10 mm by 3.5 mm by 1.5 mm, e.g., the area marked by the red-dotted line in fig. S1A) from a square-shaped HOPG sheet (fig. S1A) using a computer numerical control (CNC) milling machine (Proxxon FF 500, GmbH). Then, the cut piece was "anchored and glued" inside the recess area of an M10 screw sample holder by filling the recess with a low temperature solder alloy (Sn-43%Bi) at ~140°C (fig. S1B). The "soldering" operation was carried out by placing the M10 screw on top of a hot plate (Stuart UC152, UK). Figure S1C shows, before ULPE, the typical macrostructures of a polished HOPG sheet top surface. Figure S1 (D and E) shows that, after ULPE, the front edge of the HOPG was opened up and exfoliated into many multilayer graphite bundles. Imaging the layer bundles at higher magnification (fig. S1F), clearly, they were composed of hundreds of sub-micrometer and nano lamellae. Figure S2A shows the surface of several raw NGFs. A NGF piece was held vertically by using a small tweezer with carbon tip and then glued inside the recess area of an M10 screw sample holder (fig. S2B). The similar soldering operation was used for mounting the NGF piece. Figure S2C shows clearly that numerous defects exist on the NGF surface, which are likely sites for initiating layer exfoliation. Figure S2 (D to F) shows that, after ULPE, the top surface of the NGF was opened up and exfoliated into graphite multilayers. Such multilayers were further exfoliated into nanoflakes or multilayer graphene inside the liquid during the ULPE process.

The apparatus for the in situ ULPE experiments and sample arrangement

The experiments were carried out at the SPB/SFX instrument of the EuXFEL in Schenefeld, Germany. Figure S3 shows schematically the apparatus for the in situ ULPE experiments and sample arrangement. First, a stainless steel adapter was mounted on the sample stage (an X-Y-Z movement plus rotation stage). The ultrasound processor was mounted on another similar stage. Both can move independently. Second, the M10 screw with the mounted graphite sample (figs. S1B and S2B) was screwed from the bottom into the quartz tube (20-mm outer diameter, 80 mm tall, and 0.5 mm thick) and then water-tight sealed with the stainless steel adapter by using the Sn-43%Bi solder alloy. Third, ~15 ml of DIWater was carefully filled into the quartz tube container using a syringe. An UP100H ultrasound processor (Hielscher Ultrasonic Technology) and a Ti-6Al-4 V alloy sonotrode (MS2, 2.0-mm-diameter tip) were used to apply the ultrasound of 30 kHz into the DIWater contained inside the quartz tube container.

Megahertz x-ray microscopy and x-ray pulse train configurations

Figure S4 shows schematically the general configuration of the ULPE processing operation at the SPB/SFX instrument of the EuXFEL. X-ray beams of 20 keV were used, and each bunch of the pulse train was filled with 256 x-ray pulses. The beam from the self-amplified spontaneous emission 1 (SASE1) undulator source was delivered by the horizontal offset mirrors placed 280 m downstream of the source (fig. S4A). A YAG: Ce 20-μm scintillator was used to convert the x-rays to visible light, and the sample-to-scintillator distance was set at ~0.725 m. The x-ray pulse energy and duration measured with a gas detection monitor at the end of the SASE1 tunnel was about ~700 μJ and ~25 fs. The time interval between two consecutive pulses within one train is 886 ns, providing an intra-burst frame rate of ~1.13 MHz. The repetition frequency of the pulse trains is 10 Hz (fig. S4B).

Two Shimadzu HPV-X2 full-field cameras coupled with a 10× near ultraviolet (NUV) objective lens were used together to capture 256 images in one pulse train. The 127th and 128th images in the first camera were overlapped with the first and second images in the second camera (fig. S4B). The field of view is 1280 μm (horizontal) by 800 (vertical) μm with an effective pixel size of 3.2 μm. The ultrasound frequency is 30 kHz; hence, the 128 images (113.92 μs) recorded in each camera span over ~3.5 ultrasound cycles. After the camera memory was full, ~15 s was needed to transfer the image data into the data storage server until the next round image recording could be started. Since the NGF is much easier to be exfoliated during the ULPE process, the ultrasound was set to run for 2 s in every 13 s, i.e., synchronized with the image recording and transfer in every 15 s to capture longer timescale exfoliation dynamic. Synchronization among the triggering of the x-ray pulses, image recording, and ultrasound was achieved by using a synchronized microTCA timing board and digital delay/pulse generators (Stanford Research DG645) for setting the time delay for each event.

ML-assisted image normalization and phase segmentation

Compared to the x-ray pulses produced by modern synchrotron sources, the x-ray pulses produced by the SASE undulator at the EuXFEL have extremely high spatial coherence and much higher pulse-energy fluctuations between pulses, resulting in stochastic spatiotemporal flickering in each recorded image, and therefore notable variation in the image quality across all different datasets (*37*). For example, fig. S5 shows that the raw image has a broad range of pixel intensities and fluctuations (I_{raw}). There exist even wider fluctuations in different shots. To extract more clearly and accurately the dynamically changed shape of the bubble boundaries and the moving edges of the graphite layers recorded in different image datasets, such spatiotemporal flickering has to be removed or "smoothed out." Hence, we implemented a combined image normalization and ML-based segmentation strategy in this work, achieving highly efficiently and accurate imaging processing of the many terabit image data, which is virtually impossible by using manual or other conventional image processing methods.

First, an x-ray image (I_{raw}) (see fig. S5) collected by one camera in a pulse train was flat-field corrected on a shot-by-shot basis using ML-assisted principal components analysis (PCA) method (*38*–*40*),

producing the image (I_{PCA}). Second, a Gaussian blur filter (Sigma = 3.0) was applied to the PCA-processed image, producing the image (I_G). Last, the I_G was subtracted from the I_{PCA} to produce the image I_F, in which the bubble boundaries and the graphite layers' edges were normalized and enhanced.

After image normalization, an ML-assisted phase segmentation method [Trainable Weka Segmentation (*41*) in Fiji (*42*)] was applied to identify and segment the time-evolved features recorded in the images (here, mainly the bubbles and the exfoliated graphite layers). Figure S6 shows the workflow of a typical case. First, a region of interest (i.e., bubble or graphite layer) was cropped from the normalized x-ray images. Second, five filters (Sobel, Hessian, difference of Gaussians, Gaussian blur, and membrane projections) in Fiji were selected and used to extract the image features. The Sobel, difference of Gaussians, and Hessian filters were used as the edge enhancement. The Gaussian blur filter was used as the noise reduction. Membrane projections filter was used to localize the bubble structures of a certain size and thickness. Third, a set of pixels were artificially defined and labeled to differentiate the features. Fourth, a Weka algorithm with the FastRandomForest classifier was applied to separate these pixels. Users can also provide meaningful or sensible inputs at each iteration by correcting or adding new labels. After the training procedure and segmentation accuracy were fully validated using representative regions, then the trained models were applied to the full dataset.

Figures S7 to S12 show some representative examples of ML-assisted segmentation results (from the already comprehensively analyzed movies). Clearly, this workflow greatly enhanced the accuracy and efficiency in identifying the critical time-evolved structures across thousands of image frames, enabling reliable quantification of the time-evolved bubble dynamics and the graphite layer exfoliation due to the action of a single bubble, multi-bubbles, or bubble clouds. Although ML may not provide extra information beyond the original images, it is indispensable for us to extract and present the accurate and reliable scientific data (findings), which are critical in supporting the in-depth understanding and scientific interpretation of the results.

Multiphysics modeling of bubble dynamics, shock waves, and impacts onto graphite

Complementary to the experiments, we used the finite element analysis method and did systematic numerical simulation on (i) the bubble dynamics, (ii) the shock wave propagation, and (iii) the shock waves' impact force onto the graphite layers (i.e., the impulsive and cyclic stresses produced into the graphite layers). By feeding the quantitative experimental results into the multiphysics numerical models, we made comprehensive and systematic validation and calibration of the models, achieved high-fidelity numerical modeling in the ultrasonic exfoliation of 2D materials. More detailed descriptions are given in sections S1.1 to S1.6 of the Supplementary Materials.

Supplementary Materials

The PDF file includes:

Supplementary Text
Figs. S1 to S18
Tables S1 and S2
Legends for movies S1 to S12
References

Other Supplementary Material for this manuscript includes the following:

Movies S1 to S12

REFERENCES AND NOTES

1. C. E. Brennen, *Cavitation and Bubble Dynamics* (Oxford Univ. Press, 1995).
2. A. G. Terentiev, I. N. Kirschner, J. S. Uhlman, *The Hydrodynamics of Cavitating Flows* (Backbone Publishing Company, 2011).
3. W. Lauterborn, T. Kurz, Physics of bubble oscillations. *Rep. Prog. Phys.* **73**, 106501 (2010).
4. L. Qin, B. M. Maciejewska, T. Subroto, J. A. Morton, K. Porfyrakis, I. Tzanakis, D. G. Eskin, N. Grobert, K. Fezzaa, J. Mi, Ultrafast synchrotron x-ray imaging and multiphysics modeling of liquid phase fatigue exfoliation of graphite under ultrasound. *Carbon* **186**, 227–237 (2022).
5. L. Qin, K. Porfyrakis, I. Tzanakis, N. Grobert, D. G. Eskin, K. Fezzaa, J. Mi, Multiscale interactions of liquid, bubbles and solid phases in ultrasonic fields revealed by multiphysics modeling and ultrafast x-ray imaging. *Ultrason. Sonochem.* **89**, 106158 (2022).
6. A. K. Geim, Graphene: Status and prospects. *Science* **324**, 1530–1534 (2009).
7. K. Khan, A. K. Tareen, M. Aslam, R. Wang, Y. Zhang, A. Mahmood, Z. Ouyang, H. Zhang, Z. Guo, Recent developments in emerging two-dimensional materials and their applications. *J. Mater. Chem. C* **8**, 387–440 (2020).
8. X. Li, L. Zhi, Graphene hybridization for energy storage applications. *Chem. Soc. Rev.* **47**, 3189–3216 (2018).
9. K. S. Novoselov, V. I. Fal'ko, L. Colombo, P. R. Gellert, M. G. Schwab, K. Kim, A roadmap for graphene. *Nature* **490**, 192–200 (2012).
10. G. Cravotto, P. Cintas, Sonication-assisted fabrication and post-synthetic modifications of graphene-like materials. *Chemistry* **16**, 5246–5259 (2010).
11. L. Niu, J. N. Coleman, H. Zhang, H. Shin, M. Chhowalla, Z. Zheng, Production of two-dimensional nanomaterials via liquid-based direct exfoliation. *Small* **12**, 272–293 (2016).
12. Y. Xu, H. Cao, Y. Xue, B. Li, W. Cai, Liquid-phase exfoliation of graphene: An overview on exfoliation media, techniques, and challenges. *Nanomaterials* **8**, 942 (2018).
13. D. Parviz, F. Irin, S. A. Shah, S. Das, C. B. Sweeney, M. J. Green, Challenges in liquid-phase exfoliation, processing, and assembly of pristine graphene. *Adv. Mater.* **28**, 8796–8818 (2016).
14. Y. Hernandez, V. Nicolosi, M. Lotya, F. M. Blighe, Z. Sun, S. De, I. T. McGovern, B. Holland, M. Byrne, Y. K. Gun'Ko, J. J. Boland, P. Niraj, G. Duesberg, S. Krishnamurthy, R. Goodhue, J. Hutchison, V. Scardaci, A. C. Ferrari, J. N. Coleman, High-yield production of graphene by liquid-phase exfoliation of graphite. *Nat. Nanotechnol.* **3**, 563–568 (2008).
15. J. N. Coleman, M. Lotya, A. O'Neill, S. D. Bergin, P. J. King, U. Khan, K. Young, A. Gaucher, S. De, R. J. Smith, I. V. Shvets, S. K. Arora, G. Stanton, H. Y. Kim, K. Lee, G. T. Kim, G. S. Duesberg, T. Hallam, J. J. Boland, J. J. Wang, J. F. Donegan, J. C. Grunlan, G. Moriarty, A. Shmeliov, R. J. Nicholls, J. M. Perkins, E. M. Grieveson, K. Theuwissen, D. W. McComb, P. D. Nellist, V. Nicolosi, Two-dimensional nanosheets produced by liquid exfoliation of layered materials. *Science* **331**, 568–571 (2011).
16. V. Nicolosi, M. Chhowalla, M. G. Kanatzidis, M. S. Strano, J. N. Coleman, Liquid exfoliation of layered materials. *Science* **340**, 1226419 (2013).
17. J. A. Morton, M. Khavari, L. Qin, B. M. Maciejewska, A. V. Tyurnina, N. Grobert, D. G. Eskin, J. Mi, K. Porfyrakis, P. Prentice, I. Tzanakis, New insights into sono-exfoliation mechanisms of graphite: In situ high-speed imaging studies and acoustic measurements. *Mater. Today* **49**, 10–22 (2021).
18. B. Wang, D. Tan, T. L. Lee, J. C. Khong, F. Wang, D. Eskin, T. Connolley, K. Fezzaa, J. Mi, Ultrafast synchrotron x-ray imaging studies of microstructure fragmentation in solidification under ultrasound. *Acta Mater.* **144**, 505–515 (2018).
19. F. Wang, D. Eskin, J. Mi, C. Wang, B. Koe, A. King, C. Reinhard, T. Connolley, A synchrotron x-radiography study of the fragmentation and refinement of primary intermetallic particles in an Al-35 Cu alloy induced by ultrasonic melt processing. *Acta Mater.* **141**, 142–153 (2017).
20. S. Wang, J. Kang, Z. Guo, T. L. Lee, X. Zhang, Q. Wang, C. Deng, J. Mi, In situ high speed imaging study and modeling of the fatigue fragmentation of dendritic structures in ultrasonic fields. *Acta Mater.* **165**, 388–397 (2019).
21. A. Kaur, J. A. Morton, A. V. Tyurnina, A. Priyadarshi, A. Holland, J. Mi, K. Porfyrakis, D. G. Eskin, I. Tzanakis, Temperature as a key parameter for graphene sono-exfoliation in water. *Ultrason. Sonochem.* **90**, 106187 (2022).
22. A. V. Tyurnina, I. Tzanakis, J. Morton, J. Mi, K. Porfyrakis, B. M. Maciejewska, N. Grobert, D. G. Eskin, Ultrasonic exfoliation of graphene in water: A key parameter study. *Carbon* **168**, 737–747 (2020).
23. X. Li, X. Wang, L. Zhang, S. Lee, H. Dai, Chemically derived, ultrasmooth graphene nanoribbon semiconductors. *Science* **319**, 1229–1232 (2008).
24. A. V. Alaferdov, A. Gholamipour-Shirazi, M. A. Canesqui, Y. A. Danilov, S. A. Moshkalev, Size-controlled synthesis of graphite nanoflakes and multi-layer graphene by liquid phase exfoliation of natural graphite. *Carbon* **69**, 525–535 (2014).
25. M. Lotya, P. J. King, U. Khan, S. De, J. N. Coleman, High-concentration, surfactant-stabilized graphene dispersions. *ACS Nano* **4**, 3155–3162 (2010).
26. Z. Li, R. J. Young, C. Backes, W. Zhao, X. Zhang, A. A. Zhukov, E. Tillotson, A. P. Conlan, F. Ding, S. J. Haigh, K. S. Novoselov, J. N. Coleman, Mechanisms of liquid-phase exfoliation for the production of graphene. *ACS Nano* **14**, 10976–10985 (2020).

27. A. V. Tyurnina, J. A. Morton, T. Subroto, M. Khavari, B. Maciejewska, J. Mi, N. Grobert, K. Porfyrakis, I. Tzanakis, D. G. Eskin, Environment friendly dual-frequency ultrasonic exfoliation of few-layer graphene. *Carbon* **185**, 536–545 (2021).
28. P. Vagovič, T. Sato, L. Mikeš, G. Mills, R. Graceffa, F. Mattsson, P. Villanueva-Perez, A. Ershov, T. Faragó, J. Uličný, H. Kirkwood, R. Letrun, R. Mokso, M.-C. Zdora, M. P. Olbinado, A. Rack, T. Baumbach, J. Schulz, A. Meents, H. N. Chapman, A. P. Mancuso, Megahertz x-ray microscopy at x-ray free-electron laser and synchrotron sources. *Optica* **6**, 1106–1109 (2019).
29. J. C. P. Koliyadu, D. Mosko, E. M. Asimakopoulou, V. Bellucci, S. Birnsteinova, R. Bean, R. Letrun, C. Kim, H. Kirkwood, G. Giovanetti, N. Jardon, J. Szuba, T. Guest, A. Koch, J. Grunert, P. Szeles, P. Villanueva-Perez, F. Reuter, C. D. Ohl, M. A. Noack, F. Garcia-Moreno, Z. Kuglerova-Valdova, L. Juha, M. Nikl, W. Yashiro, H. Soyama, D. Eakins, A. M. Korsunsky, J. Ulicny, A. Meents, H. N. Chapman, A. P. Mancuso, T. Sato, P. Vagovic, Development of MHz x-ray phase contrast imaging at the European XFEL. *J. Synchrotron Radiat.* **32**, 17–28 (2025).
30. A. P. Mancuso, A. Aquila, L. Batchelor, R. J. Bean, J. Bielecki, G. Borchers, K. Doerner, K. Giewekemeyer, R. Graceffa, O. D. Kelsey, Y. Kim, H. J. Kirkwood, A. Legrand, R. Letrun, B. Manning, L. Lopez Morillo, M. Messerschmidt, G. Mills, S. Raabe, N. Reimers, A. Round, T. Sato, J. Schulz, C. Signe Takem, M. Sikorski, S. Stern, P. Thute, P. Vagovic, B. Weinhausen, T. Tschentscher, The single particles, clusters and biomolecules and serial femtosecond crystallography instrument of the European XFEL: Initial installation. *J. Synchrotron Radiat.* **26**, 660–676 (2019).
31. M. Khavari, A. Priyadarshi, A. Hurrell, K. Pericleous, D. Eskin, I. Tzanakis, Characterization of shock waves in power ultrasound. *J. Fluid Mech.* **915**, R3 (2021).
32. M. J. McAllister, J.-L. Li, D. H. Adamson, H. C. Schniepp, A. A. Abdala, J. Liu, M. Herrera-Alonso, D. L. Milius, R. Car, R. K. Prud'homme, Single sheet functionalized graphene by oxidation and thermal expansion of graphite. *Chem. Mater.* **19**, 4396–4404 (2007).
33. S. R. Snyder, W. W. Gerberich, H. S. White, Scanning-tunneling-microscopy study of tip-induced transitions of dislocation-network structures on the surface of highly oriented pyrolytic graphite. *Phys. Rev. B* **47**, 10823–10831 (1993).
34. Q. Zheng, B. Jiang, S. Liu, Y. Weng, L. Lu, Q. Xue, J. Zhu, Q. Jiang, S. Wang, L. Peng, Self-retracting motion of graphite microflakes. *Phys. Rev. Lett.* **100**, 067205 (2008).
35. Z. Liu, J. Yang, F. Grey, J. Z. Liu, Y. Liu, Y. Wang, Y. Yang, Y. Cheng, Q. Zheng, Observation of microscale superlubricity in graphite. *Phys. Rev. Lett.* **108**, 205503 (2012).
36. D. E. Soule, C. W. Nezbeda, Direct basal-plane shear in single-crystal graphite. *J. Appl. Phys.* **39**, 5122–5139 (1968).
37. T. W. Guest, R. Bean, J. Bielecki, S. Birnsteinova, G. Geloni, M. Guetg, R. Kammering, H. J. Kirkwood, A. Koch, D. M. Paganin, G. van Riessen, P. Vagovic, R. de Wijn, A. P. Mancuso, B. Abbey, Shot-to-shot two-dimensional photon intensity diagnostics within megahertz pulse-trains at the European XFEL. *J. Synchrotron Radiat.* **29**, 939–946 (2022).
38. V. Van Nieuwenhove, J. De Beenhouwer, F. De Carlo, L. Mancini, F. Marone, J. Sijbers, Dynamic intensity normalization using eigen flat fields in X-ray imaging. *Opt. Express* **23**, 27975–27989 (2015).
39. S. Birnsteinova, D. E. F. de Lima, E. Sobolev, H. J. Kirkwood, V. Bellucci, R. J. Bean, C. Kim, J. C. Koliyadu, T. Sato, F. Dall'Antonia, Online dynamic flat-field correction for MHz microscopy data at European XFEL. arXiv:2303.18043 [physics.ins-det] (2023).
40. K. Buakor, Y. Zhang, Š. Birnšteinová, V. Bellucci, T. Sato, H. Kirkwood, A. P. Mancuso, P. Vagovic, P. Villanueva-Perez, Shot-to-shot flat-field correction at x-ray free-electron lasers. *Opt. Express* **30**, 10633–10644 (2022).
41. I. Arganda-Carreras, V. Kaynig, C. Rueden, K. W. Eliceiri, J. Schindelin, A. Cardona, H. Sebastian Seung, Trainable Weka segmentation: A machine learning tool for microscopy pixel classification. *Bioinformatics* **33**, 2424–2426 (2017).
42. C. A. Schneider, W. S. Rasband, K. W. Eliceiri, NIH Image to ImageJ: 25 years of image analysis. *Nat. Methods* **9**, 671–675 (2012).
43. S. T. Miller, H. Jasak, D. A. Boger, E. G. Paterson, A. Nedungadi, A pressure-based, compressible, two-phase flow finite volume method for underwater explosions. *Comput. Fluids* **87**, 132–143 (2013).
44. M. van Sint Annaland, N. Deen, J. Kuipers, Numerical simulation of gas bubbles behaviour using a three-dimensional volume of fluid method. *Chem. Eng. Sci.* **60**, 2999–3011 (2005).
45. B. Van Wachem, A.-E. Almstedt, Methods for multiphase computational fluid dynamics. *Chem. Eng. J.* **96**, 81–98 (2003).
46. S. O. Catarino, J. M. Miranda, S. Lanceros-Mendez, G. Minas, Numerical prediction of acoustic streaming in a microcuvette. *Can. J. Chem. Eng.* **92**, 1988–1998 (2014).
47. Y. Li, J. Zhang, L.-S. Fan, Discrete-phase simulation of single bubble rise behavior at elevated pressures in a bubble column. *Chem. Eng. Sci.* **55**, 4597–4609 (2000).
48. J. U. Brackbill, D. B. Kothe, C. Zemach, A continuum method for modeling surface tension. *J. Comput. Phys.* **100**, 335–354 (1992).
49. B. Lafaurie, C. Nardone, R. Scardovelli, S. Zaleski, G. Zanetti, Modelling merging and fragmentation in multiphase flows with SURFER. *J. Comput. Phys.* **113**, 134–147 (1994).
50. J. Yin, Y. Zhang, J. Zhu, Y. Zhang, S. Li, On the thermodynamic behaviors and interactions between bubble pairs: A numerical approach. *Ultrason. Sonochem.* **70**, 105297 (2021).
51. H. Yu, L. Goldsworthy, P. Brandner, J. Li, V. Garaniya, Modelling thermal effects in cavitating high-pressure diesel sprays using an improved compressible multiphase approach. *Fuel* **222**, 125–145 (2018).
52. P. Koukouvinis, M. Gavaises, O. Supponen, M. Farhat, Simulation of bubble expansion and collapse in the vicinity of a free surface. *Phys. Fluids* **28**, 052103 (2016).
53. P. Koukouvinis, M. Gavaises, O. Supponen, M. Farhat, Numerical simulation of a collapsing bubble subject to gravity. *Phys. Fluids* **28**, 032110 (2016).
54. S. Qiu, X. Ma, B. Huang, D. Li, G. Wang, M. Zhang, Numerical simulation of single bubble dynamics under acoustic standing waves. *Ultrason. Sonochem.* **49**, 196–205 (2018).
55. L. P. Gor'Kov, On the forces acting on a small particle in an acoustical field in an ideal fluid. *Sov. Phys. Dokl.* **6**, 773–775 (1962).
56. A. A. Doinikov, Acoustic radiation pressure on a compressible sphere in a viscous fluid. *J. Fluid Mech.* **267**, 1–22 (1994).
57. W. Wei, D. B. Thiessen, P. L. Marston, Acoustic radiation force on a compressible cylinder in a standing wave. *J. Acoust. Soc. Am.* **116**, 201–208 (2004).
58. F. G. Mitri, Axial time-averaged acoustic radiation force on a cylinder in a nonviscous fluid revisited. *Ultrasonics* **50**, 620–627 (2010).
59. G. T. Silva, An expression for the radiation force exerted by an acoustic beam with arbitrary wavefront (L). *J. Acoust. Soc. Am.* **130**, 3541–3544 (2011).
60. K. Yosioka, Y. Kawasima, Acoustic radiation pressure on a compressible sphere. *Acust.* **5**, 167–173 (1955).
61. V. A. D. Grosso, Speed of sound in pure water. *J. Acoust. Soc. Am.* **52**, 1442–1446 (1972).
62. A. S. M. Sohaimi, M. S. Risby, S. A. F. M. Ishak, S. Khalis, M. N. Norazman, I. Ariffin, M. A. Yusof, Using computational fluid dynamics (CFD) for blast wave propagation under structure. *Procedia Comput. Sci.* **80**, 1202–1211 (2016).
63. L. Yang, J. Xiang, S. Zhang, H. Kang, X. Wang, W. Xia, Compressibility effects on cavity dynamics and shock waves in high-speed water entry. *Phys. Fluids* **36**, 042104 (2024).
64. K. Yasui, T. Kozuka, T. Tuziuti, A. Towata, Y. Iida, J. King, P. Macey, FEM calculation of an acoustic field in a sonochemical reactor. *Ultrason. Sonochem.* **14**, 605–614 (2007).
65. D. Dhande, G. Lanjewar, D. Pande, Implementation of CFD–FSI technique coupled with response surface optimization method for analysis of three-lobe hydrodynamic journal bearing. *J. Inst. Eng. (India): C* **100**, 955–966 (2019).
66. H.-H. Lee, *Finite Element Simulations with ANSYS Workbench 2023: Theory, Applications, Case Studies* (SDC publications, 2023).
67. S. Patankar, *Numerical Heat Transfer and Fluid Flow* (Taylor & Francis, 2018).
68. P. K. Khosla, S. G. Rubin, A diagonally dominant second-order accurate implicit scheme. *Comput. Fluids* **2**, 207–209 (1974).
69. G. Papadakis, G. Bergeles, Locally modified second order upwind scheme for convection terms discretization. *Int. J. Numer. Methods Heat Fluid Flow* **5**, 49–62 (1995).
70. E. F. Toro, *Riemann Solvers and numerical Methods for fluid Dynamics. A practical Introduction. 2nd ed*. (Riemann solvers and numerical methods for fluid dynamics. A practical introduction. ed. 2, 1999).
71. A. Inc, ANSYS Fluent Theory Guide (2013).
72. L. Qin, K. Xiang, L. Li, I. Tzanakis, D. Eskin, J. Mi, An integrated numerical modelling framework for simulation of the multiphysics in sonoprocessing of materials. *Ultrason. Sonochem.* **120**, 107428 (2025).
73. G. B. Lebon, I. Tzanakis, K. Pericleous, D. Eskin, Experimental and numerical investigation of acoustic pressures in different liquids. *Ultrason. Sonochem.* **42**, 411–421 (2018).
74. I. Tzanakis, G. Lebon, D. Eskin, K. Pericleous, Characterizing the cavitation development and acoustic spectrum in various liquids. *Ultrason. Sonochem.* **34**, 651–662 (2017).

Acknowledgments: We acknowledge the EuXFEL in Schenefeld, Germany, for provision of the x-ray free-electron laser beamtime (proposal no. 3100, the first user experiment was conducted between 15 to 18 September 2022), and the staff at the SPB/SFX SASE1 instrument for technical assistance. P.V. would like to acknowledge the technical support of T. Dietze. **Funding:** This study was supported by UK-EPSRC grants (EP/R031819/, EP/R031665/1, EP/R031401/1, and EP/R031975/1), the Internal EuXFEL R&D project "MHz microscopy at EuXFEL: From demonstration to method" (2020 – 2022, HORIZON-EIC-2021-PATHFINDEROPEN-01-01), the MHz-TOMOSCOPY project (grant agreement: 101046448), and the Doctoral Scholarship offered by the University of Hull and China Scholarship Council (202108500033). **Author contributions:** Conceptualization: J.M. Methodology: K.X., L.Q., S.H., H.S., J.M., and P.V. Conceiving and establishment of MHz imaging method and apparatus at SPB/SFX instrument: P.V. Sample preparation: K.X., S.H., H.S., E.R., V.Ba., A.S., and J.M. Investigation: K.X., S.H., J.M., V.Be., S.B., R.D.W., J.C.P.K., F.H.M.K., A.R., T.S., M.S., Y.Z., E.M.A., P.V.-P., R.B., P.V., and A.P.M. Data analysis: K.X., L.Q., S.B., Y.Z., P.V.-P., and J.M. Funding acquisition: K.P., I.T., D.G.E., N.G., and J.M. Writing—original draft: K.X., L.Q., and J.M. Writing—review and editing: K.X., L.Q., J.M., J.C.P.K, D.G.E., K.P., and A.P.M. **Competing interests:** The authors declare that they have no competing interests. **Data and materials availability:** All data needed to evaluate the conclusions in the paper are present in the paper and/or the Supplementary Materials. Data recorded for the experiment at the European XFEL are available at DOI: 10.22003/XFEL.EU-DATA-003100-00.

Submitted 12 May 2025
Accepted 29 October 2025
Published 28 November 2025
10.1126/sciadv.ady9558